Research Article

Heat and mass transfer in stagnation point flow of cross nanofluid over a permeable extending/contracting surface: A stability analysis

H. Thameem BASH[1], R. SIVARAJ[1,*]

[1]Department of Mathematics, School of Advanced Sciences, Vellore Institute of Technology, Vellore-632014, India.

ABSTRACT

This work aims at examining the thermophoresis and Brownian motion characteristics on the stagnation point flow of Cross nanofluid over a permeable stretching /contracting surface. Flow equations are modelled by means of the Buongiorno nanofluid model. The transformed non-linear fluid transport equations are solved numerically through Runge-Kutta Fehlberg (RKF) approach. The temporal stability test is executed to reveal the behaviour of dual solution that arises for various initial guesses. To validate the present model, first and second solutions are compared with earlier published works which found good agreement. The fluctuations of velocity, heat and mass transfer distributions are scrutinized through the graphs with active parameters such as Wessienburg number, Brownian motion, Eckert number, and thermophoresis. The results exposed that the Brownian motion declines the rate of heat transfer for the first solution. Cross nanofluid velocity amplifies by rising Weissenberg number. By the impact of Eckert number, the second solution has a higher magnitude than the first solution. For the first solution, the cross nanofluid velocity rises when increasing the suction/injection parameter.

Cite this article as: Bash H T, Sivaraj R. Heat and mass transfer in stagnation point flow of cross nanofluid over a permeable extending/contracting surface: A stability analysis. J Ther Eng 2022;8(1):38–51.

INTRODUCTION

Efficient heat dissipation process is one of the significant aspects of energy management in engineering and technology. In the past decades, broad exploration has been done to notice the promising ways to augment energy conversion in various utilizations. Nanofluids are noticed as suitable fluids to provide such a promising approach for efficient energy management. Nanofluids are the fluids which contain nanosize particles suspended in regular heat transfer fluids. Nanofluids offer higher heat dissipation compared to regular fluids since the suspended solid particles have high thermal conductivity. Existing literature in the field of nanofluids manifests that nanofluids can be

---

***Corresponding author.**
*E-mail address: sivaraj.kpm@gmail.com

utilized to augment the heat transfer in extensive applications like cooling of computers or CPUs, manufacturing or machining processes, solar energy collectors, nuclear reactors, electronic equipment, bio-medical and radiator cooling [1-3]. Several models have been presented to investigate the nanofluids. The Buongiorno model is one of the nanofluid models, which is adopted by many researchers to study the nanofluids. Buongiorno [4] model consists of the momentum, heat and mass transport equations with the influence of Brownian motion and thermophoretic diffusivity. Basha et al. [5] used the Crank Nicolson approach to address the time-dependent flow of chemically reacting nanofluid in the presence of irregular heat source/sink, Brownian motion and thermophoresis (slip mechanisms). Pal et al. [6] explored the viscoelastic nanofluid flow bounded by a stretchable surface by considering thermophoresis and Brownian motion and found that thermal related boundary layer rises for escalating the thermophoresis and Brownian motion. Mittal and Patel [7] employed Buongiorno nanofluid model to model the flow of Casson nanofluid over a permeable plate and noticed that nanofluid velocity increases with an increase in Casson fluid parameter. Flow behaviour and entropy generation of peristaltic flow of a viscoelastic nanofluid in nonuniform annuli with slip mechanisms are addressed by Riaz et al. [8] and found that the pumping rate elevates by Grashof number. Several researchers explored the slips mechanisms in various aspects which are shown in Refs. [9-13].

Fluid flow over an extending/contracting surface has significant uses in industries like wire drawing, aerodynamics, glass blowing, hot rolling, extrusion of plastic sheets, crystal growing, manufacturing of plastic and condensation process. Khan et al. [14] conducted the temporal stability performance on the ethylene glycol-based flow of Al_2O_3 nanofluid in the presence of surface extending behaviour and exposed that the second outcome is unrealizable in nature. Pop et al. [15] discussed the heat transfer characteristics of nanofluid (Cu, Al_2O_3 and TiO_2 water) over a stretching/contracting porous surface and found that the Cu nanoparticles amplify fluid temprature. Mahapatra and Sidui [16] carried out a numerical study which is aimed to express the heat transfer characteristics of time dependent viscous fluid flow over an expanding/contracting surface and presented that the rate of heat transfer is increased at the wall as the time-dependent parameter increases. Hashim et al. [17] demonstrated the Carreau fluid rheological model transport behaviour on the flow of time-related nanofluid over a disk with expanding/contracting surface and pointed out that primary and secondary solutions have reverse behaviour in nanofluid velocity. Hamid et al. [18] utilized the Runge-Kutta Fehlberg Approach to explore the fluid transport characteristics of Williamson fluid over an expanding/contracting surface. Alam et al. [19] explained the impacts of variable viscosity, variable Prandtl number and variable Schmidt number on time-dependent viscous

fluid over a permeable expanding/contracting wedge. Bachok et al. [20] reported the dual nature of viscous fluid over a melting expanding/contracting sheet with Lorentz force and showed that the Lorentz force diminishes the fluid velocity and temperature for the upper solution. The heat transfer behaviour of Cu/water nanofluid flow over a stretching/shrinking channel with the use of Duan–Rach approach is explored by Dogonchi and Ganji [21].

The non-Newtonian fluid is a viscous shear-dependent fluid with shear-thinning or shear-thickening characteristics. Paints, lubricants, ketchup, silly putty, blood, and toothpaste are some of the examples for non-Newtonian fluids. Many researchers have proposed different rheological models to characterize the non-Newtonian fluids, which include, Cross fluid, Carreau fluid, Maxwell fluid, Walters B-fluid, Casson fluid, and Williamson fluid. Several authors investigated different types of non-Newtonian models in various aspects [22-25]. Cross fluid (power-law index with very low and very high shear rates) is one of sub class of non-Newtonian fluids and this model was proposed by Cross [26]. Due to the significance in exploring the blood behaviour, Cross fluid model has received notable attention; further this model affords 0.40% aqueous solution of polyacrylamide, 0.35% aqueous solution of Xanthan gum. In addition, the presence of time constant in Cross fluid model has widespread uses in engineering calculations. Abbas et al [27] utilized the Buongiorno nanofluid model to explore fluid transport properties and entropy generation of Cross nanofluid with linear radiation and observed that varying thermophoretic parameter enhances temperature and mass transfer of nanofluid. Khan et al. [28] scrutinized the impact of nonlinear radiation on Cross nanofluid by using Buongiorno nanofluid model and found that increasing values of Brownian motion parameter declines the mass transfer. Alam et al. [29] addressed the impact of activation energy on Cross nanofluid over an expanding disk with Navier slip. Shahzad et al. [30] explored the Cross nanofluid transport properties and entropy generation with linear radiation, Hall current, and chemical reaction and noticed that the total entropy generation enhances for increasing linear radiation.

Previously, researchers have investigated the Cross fluid model with various effects like radiation, activation energy, magnetic field and entropy generation over an extending/contracting sheet. In the present model, we have examined the dual natures and temporal stability of Cross nanofluid over a permeable extending/contracting surface. From a significant review of the current literature, it is noticed that no attempt has been made to report the Cross nanofluid dual natures and stability analysis in the presence of viscous dissipation and slip mechanisms. The suitable self-similarity variables are employed to reduce the partial differential equations into ordinary differential equations. Further, the solutions of the transformed equations are obtained by means of *RKF* method. It is worth to note that there are

two solutions exist for extending/contracting surface cases. To verify the obtained numerical solutions, the comparison is done with the existing results in the literature for two solutions. The outcomes of emerging parameters on velocity, temperature, and concentration have been reveled via graphs for both solutions.

MATHEMATICAL FORMULATION

In formulating the present model, we have considered two dimensional, stagnation point, steady flow of Cross nanofluid over a permeable extending/contracting surface. The physical model of this problem is shown in Fig. 1. λ_T is the extending/contracting surface parameter and it is noticed that the positive values of λ_T represents the extension of the surface and the negative values of λ_T represents the contracting of the surface. The Cartesian coordinate system is considered in which x-axis is assumed to have permeable and extending/contracting nature and it is set in the flow direction whereas the y-axis is normal to the flow direction. The wall temperature (T_w) and concentration (C_w) are constants which are greater than the ambient temperature (T_∞) and ambient concentration (C_∞), respectively. $u_w = kx$ is the velocity of extending/contracting surface where positive and negative values of k indicates extending and contracting natures of the surface, respectively. Cross nanofluid transport equations are modeled by means of Buongiorno nanofluid model. By these assumption, the flow field equations are written as follows:

$$\frac{\partial u}{\partial x} + \frac{\partial v}{\partial y} = 0,$$ (1)

$$u\frac{\partial u}{\partial x} + v\frac{\partial u}{\partial y} = u_e \frac{du_e}{dx} + v_f \frac{\partial^2 u}{\partial y^2}$$
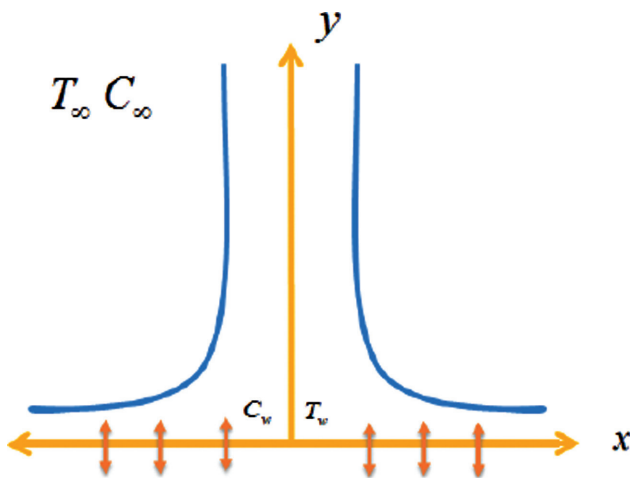
**Figure 1.** Flow geometry of the problem.

$$\left[\frac{1}{1+\left(\Gamma\frac{\partial u}{\partial y}\right)^{n_k}}\right] + v_f \frac{\partial u}{\partial y}\frac{\partial}{\partial y}\left[\frac{1}{1+\left(\Gamma\frac{\partial u}{\partial y}\right)^{n_k}}\right],$$ (2)

$$u\frac{\partial T}{\partial x} + v\frac{\partial T}{\partial y} = \alpha^* \frac{\partial^2 T}{\partial y^2} + \tau\left[D_B \frac{\partial T}{\partial y}\frac{\partial C}{\partial y} + \frac{D_T}{T_\infty}\left(\frac{\partial T}{\partial y}\right)^2\right]$$

$$+ \frac{v_f}{\left(C_P\right)_f}\left(\frac{\partial u}{\partial y}\right)^2\left(\frac{1}{1+\left(\Gamma\frac{\partial u}{\partial y}\right)^{n_k}}\right),$$ (3)

$$u\frac{\partial C}{\partial x} + v\frac{\partial C}{\partial y} = D_B \frac{\partial^2 C}{\partial y^2} + \frac{D_T}{T_\infty}\frac{\partial^2 T}{\partial y^2}.$$ (4)

The boundary conditions are given by

$$\begin{aligned}
u &= u_w(x)\lambda_T, \ v = V_w, \ T = T_w, \ C = C_w \quad \text{at} \ \ y = 0, \\
u &= u_e(x), \ T \to T_\infty, \ C \to C_\infty \quad \quad \quad \text{as} \ \ y \to \infty.
\end{aligned}$$ (5)

where $u_e = bx$ is the free stream velocity, b is a constant,

$$v_f = \frac{\mu_f}{\rho_f}, \alpha^* = \frac{k_f}{\left(\rho C_P\right)_f}, \tau = \frac{\left(\rho C_P\right)_p}{\left(\rho C_P\right)_f}.$$

Introducing the following non-dimensional variables

$$\left.\begin{aligned}
\eta &= y\left(\frac{b}{v_f}\right)^{\frac{1}{2}}, u = f'(\eta)bx, v = -f(\eta)\left(bv_f\right)^{\frac{1}{2}}, \\
T &= \left(T_w - T_\infty\right)\theta(\eta) + T_\infty, C = \left(C_w - C_\infty\right)\chi(\eta) + C_\infty.
\end{aligned}\right\}$$ (6)

The flow equations (1)-(4) with boundary conditions (equation (5)) in dimensionless form by using equation (6), which is written as follows

$$f'''\left(1+\left(1-n_k\right)\left(Wef''\right)^{n_k}\right)+\left(1+\left(Wef''\right)^{n_k}\right)^2$$
$$\left(1-\left(f'\right)^2 + ff''\right) = 0,$$ (7)

$$\theta''+\Pr\left(f\theta' + N_T\left(\theta'\right)^2 + N_B\theta'\chi' + \frac{E_c\left(f''\right)^2}{1+\left(Wef''\right)^{n_k}}\right)=0, \quad (8)$$

$$\chi''+Sc\left(f\chi' + \frac{N_T}{N_B}\theta''\right)=0.$$ (9)

and the boundary conditions become

$$f(\eta) = f_w, \ f'(\eta) = \lambda_T, \ \theta(\eta) = 1, \ \chi(\eta) = 1$$
$$\text{at} \ \ \eta = 0,$$
$$f'(\eta) = 1, \ \ \theta(\eta) \to 0, \ \ \chi(\eta) \to 0,$$
$$\text{as} \ \ \eta \to \infty. \tag{10}$$

where $\quad We = \sqrt{\dfrac{\Gamma^2 b^3 x^2}{\nu_f}}, \Pr = \dfrac{\nu_f}{\alpha^*}, N_B = \dfrac{\tau D_B (C_w - C_\infty)}{\nu_f},$

$, N_T = \dfrac{\tau D_T (T_w - T_\infty)}{T_\infty \nu_f}, E_c = \dfrac{b^2 x^2}{(C_p)_f (T_w - T_\infty)}$ and $Sc = \dfrac{\nu_f}{D_B}.$

The dimensionless local skin friction coefficient (C_f^*), dimensionless local rate of heat transfer (Nu^*) and dimensionless local rate of mass transfer (Sh^*) at the wall are defined as

$$C_f^* \operatorname{Re}^{\frac{1}{2}} = \dfrac{f''(0)}{\left(1 + \left(Wef''(0)\right)^{n_k}\right)},$$
$$Nu^* \operatorname{Re}^{\frac{1}{2}} = -\theta'(0), \tag{11}$$
$$Sh^* \operatorname{Re}^{\frac{1}{2}} = -\chi'(0).$$

STABILITY TEST

Based on the performance of Makinde [31,32], the temporal stability test is executed in this study. They revealed that the upper branch (second) solution is unrealisable, whereas the lower branch (first) solutions are stable. We have introduced a variable τ^* (dimensionless time-dependent) in the governing equations to perform the stability test. Thus the following equations are obtained

$$\nu_f \left(\dfrac{\partial u}{\partial t} + u \dfrac{\partial u}{\partial x} + v \dfrac{\partial u}{\partial y} \right) = \dfrac{u_e}{\nu_f} \dfrac{du_e}{dx} + \dfrac{\partial^2 u}{\partial y^2}$$
$$\left[\dfrac{1}{1 + \left(\Gamma \dfrac{\partial u}{\partial y} \right)^{n_k}} \right] + \dfrac{\partial u}{\partial y} \dfrac{\partial}{\partial y} \left[\dfrac{1}{1 + \left(\Gamma \dfrac{\partial u}{\partial y} \right)^{n_k}} \right], \tag{12}$$

$$(\rho C_p)_f \left(\dfrac{\partial T}{\partial t} + u \dfrac{\partial T}{\partial x} + v \dfrac{\partial T}{\partial y} \right) = \dfrac{\alpha^*}{(C_p)_f} \dfrac{\partial^2 T}{\partial y^2} + \dfrac{(\rho C_p)_p}{(\rho C_p)_f}$$
$$\left[D_B \dfrac{\partial T}{\partial y} \dfrac{\partial C}{\partial y} + \dfrac{D_T}{T_\infty} \left(\dfrac{\partial T}{\partial y} \right)^2 \right] + \mu_f \left(\dfrac{\partial u}{\partial y} \right)^2 \left(\dfrac{1}{1 + \left(\Gamma \dfrac{\partial u}{\partial y} \right)^{n_k}} \right), \tag{13}$$

$$\dfrac{\partial C}{\partial t} + u \dfrac{\partial C}{\partial x} + v \dfrac{\partial C}{\partial y} = D_B \dfrac{\partial^2 C}{\partial y^2} + \dfrac{D_T}{T_\infty} \dfrac{\partial^2 T}{\partial y^2}. \tag{14}$$

and the new self-similarity variables are as follows

$$\left. \begin{aligned} &\eta = y \left(\dfrac{b}{\nu_f} \right)^{\frac{1}{2}}, \quad u = f'(\eta, \tau^*) bx, \quad \tau^* = bt, \\ &\qquad\qquad v = -f(\eta, \tau^*)(b\nu_f)^{\frac{1}{2}}, \\ &T = T_\infty + (T_w - T_\infty)\theta(\eta, \tau^*), \ C = C_\infty \\ &\qquad\qquad + (C_w - C_\infty)\chi(\eta, \tau^*). \end{aligned} \right\} \tag{15}$$

Equations (12)-(14) are reduced by applying new self-similarity variable (equation (15)), which is written as follows

$$\dfrac{\partial^3 f}{\partial \eta^3} \left(1 + (1 - n_k) \left(We \dfrac{\partial^2 f}{\partial \eta^2} \right)^{n_k} \right) + \left(1 + \left(We \dfrac{\partial^2 f}{\partial \eta^2} \right)^{n_k} \right)^2$$
$$\left(1 - \left(\dfrac{\partial f}{\partial \eta} \right)^2 + f \dfrac{\partial^2 f}{\partial \eta^2} - \dfrac{\partial^2 f}{\partial \eta \partial \tau^*} \right) = 0, \tag{16}$$

$$\dfrac{\partial^2 \theta}{\partial \eta^2} + \Pr \left(f \dfrac{\partial \theta}{\partial \eta} + N_T \left(\dfrac{\partial \theta}{\partial \eta} \right)^2 + N_B \dfrac{\partial \theta}{\partial \eta} \dfrac{\partial \chi}{\partial \eta} + \right.$$
$$\left. \dfrac{E_c \left(\dfrac{\partial^2 f}{\partial \eta^2} \right)^2}{1 + \left(We \dfrac{\partial^2 f}{\partial \eta^2} \right)^{n_k}} - \dfrac{\partial \theta}{\partial \tau^*} \right) = 0, \tag{17}$$

$$\dfrac{\partial^2 \chi}{\partial \eta^2} + Sc \left(f \dfrac{\partial \chi}{\partial \eta} + \dfrac{N_T}{N_B} \dfrac{\partial^2 \theta}{\partial \eta^2} - \dfrac{\partial \chi}{\partial \tau^*} \right) = 0. \tag{18}$$

and boundary conditions become

$$f(0, \tau^*) = f_w, \ f'(0, \tau^*) = \lambda_T,$$
$$\theta(0, \tau^*) = 1, \ \chi(0, \tau^*) = 1 \quad \text{at} \ \eta = 0,$$
$$f'(\eta, \tau^*) = 1, \ \theta(\eta, \tau^*) \to 0,$$
$$\chi(\eta, \tau^*) \to 0 \quad \text{as} \ \eta \to \infty. \tag{19}$$

Following perturbation technique is used to perform stability test

$$f = f_0(\eta), \ \theta = \theta_0(\eta) \ \text{and} \ \chi = \chi_0(\eta)$$

with below conditions

$$\left.\begin{array}{l} f\left(\eta,\tau^*\right)=f_0\left(\eta\right)+e^{-\gamma\tau^*}F\left(\eta\right), \\ \theta\left(\eta,\tau^*\right)=\theta_0\left(\eta\right)+e^{-\gamma\tau^*}S\left(\eta\right), \\ \chi\left(\eta,\tau^*\right)=\chi_0\left(\eta\right)+e^{-\gamma\tau^*}P\left(\eta\right). \end{array}\right\} \quad (20)$$

where γ is an unidentified eigenvalue, $f_0(\eta)$, $\theta_0(\eta)$ and $\chi_0(\eta)$ are higher relative to $F(\eta)$, $S(\eta)$ and $P(\eta)$, respectively. By employing equation (20) into equations (16)-(19), the following system of equations are obtained:

$$F''' + 2F''We\left(1+We\,f_0''\right)$$
$$\left(F f_0'' + f_0 F'' - 2f_0' F' + \gamma F'\right) = 0, \quad (21)$$

$$\frac{1}{Pr}S'' + S'\left(f_0 + N_B\chi_0' + 2N_T\theta_0'\right) +$$
$$F\theta_0' + N_B\theta_0' P' + \frac{2E_c f_0''}{We} + \gamma S = 0, \quad (22)$$

$$\frac{1}{Sc}P'' + f_0 P' + F\chi_0' + \frac{N_T}{N_B}S'' + \gamma P = 0. \quad (23)$$

along with the boundary conditions

$$F(\eta) = 0, \quad F'(\eta) = 0, \quad S(\eta) = 0,$$
$$P(\eta) = 0 \quad \text{at} \quad \eta = 0,$$
$$F'(\eta) = 0, \quad S(\eta) \to 0,$$
$$P(\eta) \to 0 \quad \text{as} \quad \eta \to \infty. \quad (24)$$

The eigenvalue problem is solved numerically for specific values of $Pr = 1.2$, $We = 0.8$, $f_w = 0.1$, $Sc = 1$, $N_T = 0.2$, $E_c = 0.2$, $\lambda_T = -1.25$ and $N_B = 0.3$ and the infinite set ($\gamma_1 < \gamma_2 < \gamma_3 < ....$) of eigenvalues are received. The power-law (n_k) value is chosen as 1 [33]. It is to be noted that the solution is stable when γ is positive whereas the solution is unstable when γ is negative. Harris et al. [34] stated that normalization of a suitable boundary condition on $F(\eta)$ or $S(\eta)$ or $P(\eta)$ helps calculate the eigenvalues. The condition $F'(\eta) \to 0$ as $\eta \to \infty$ is normalized and new condition $F''(0) = 1$ is employed to solve the governing equations (21)-(23) with boundary conditions (equation (24)) in the this model.

NUMERICAL METHOD AND CODE VALIDATION

The reduced equations (equations. (7)-(9)) with the limiting condition (equation. (10)) are solved using the Runge-Kutta Fehlberg approach. In this approach, the boundary value problem (BVP) is converted into an initial value problem (IVP).

$$\frac{\overline{y_{m+1}} - \overline{y_m}}{h} = t_0\frac{25}{216} + t_2\frac{1408}{2565} + t_3\frac{2197}{4109} - t_4\frac{1}{5}, \quad (25)$$

$$\frac{\overline{y_{m+1}} - \overline{y_m}}{h} = t_0\frac{16}{135} + t_2\frac{6656}{12825} + t_3\frac{28561}{56430}$$
$$- t_4\frac{9}{50} + \frac{2}{55}t_5, \quad (26)$$

where equations (25) and (26) are the 4th and 5th order approximations to the solution respectively.

The expressions for t_0, t_1, t_2, t_3, t_4, t_5 are as follows

$$\begin{cases} \dfrac{t_0}{f} = \overline{x_m} + \overline{y_m}, \\[2mm] \dfrac{t_1}{f} = \overline{x_m} + \dfrac{h}{4}, \overline{y_m} + \dfrac{ht_0}{4}, \\[2mm] \dfrac{t_2}{f} = \overline{x_m} + \dfrac{3h}{8}, \overline{y_m} + \dfrac{3ht_0}{32} + \dfrac{9ht_1}{32}, \\[2mm] \dfrac{t_3}{f} = \overline{x_m} + \dfrac{12h}{13}, \overline{y_m} + \dfrac{1932ht_0}{2197} - \dfrac{7200ht_1}{2197} + \dfrac{7296ht_2}{2197}, \\[2mm] \dfrac{t_4}{f} = \overline{x_m} + h, \overline{y_m} + \dfrac{439ht_0}{216} - 8ht_1 + \dfrac{3860ht_2}{513} - \dfrac{845ht_3}{4104}, \\[2mm] \dfrac{t_5}{f} = \overline{x_m} + \dfrac{h}{2}, \overline{y_m} - \dfrac{8ht_0}{27} + 2ht_1 - \dfrac{3544ht_2}{2565} + \dfrac{1859ht_3}{4104} \\[4mm] \qquad\qquad - \dfrac{11ht_4}{40}, \end{cases} \quad (27)$$

Here, equation (27) is the steps of the Runge-Kutta Fehlberg approach. A new set of below mentioned variables are employed for computation

$$\begin{array}{l} f = a_1, \quad f' = a_2, \quad f'' = a_3, \quad f''' = a_3' \\ \theta = a_4, \quad \theta' = a_5, \quad \theta'' = a_5', \quad \chi = a_6, \quad \chi' = a_7, \quad \chi'' = a_7' \end{array} \quad (28)$$

applying equation (28) in equations (7)-(10), the reduced equations are as follows

$$a_3'\left(1+(1-n_k)(Wea_3)^{n_k}\right)+\left(1+(Wea_3)^{n_k}\right)^2$$
$$\left(1-(a_2)^2 + a_1 a_2\right) = 0, \quad (29)$$

$$a_5' + Pr\left(a_1 a_5 + N_T(a_5)^2 + N_B a_5 a_7\right.$$
$$\left.+ \frac{E_c(a_3)^2}{1+(Wea_3)^{n_k}}\right) = 0, \quad (30)$$

$$a_7' + Sc\left(a_1 a_7 + \frac{N_T}{N_B}a_5'\right) = 0. \quad (31)$$

with the corresponding boundary conditions

$$a_1(\eta) = f_w, \; a_2(\eta) = \lambda_T, \; a_4(\eta) = 1, \; a_6(\eta) = 1 \text{ at } \eta = 0,$$
$$a_2(\eta) = 1, \quad a_4(\eta) \to 0, \quad a_6(\eta) \to 0, \qquad \text{as } \eta \to \infty. \tag{32}$$

The reduced equations (29)-(31) with the boundary conditions(equation (32)) are solved via the Runge Kutta method, and the physical quantities (equation (11)) are also taken into consideration. The step size in the numerical solution is fixed as 0.001 ($\eta = 0.001$). Ten-decimal 1×10^{-10} places accuracy is fixed for the criterion of convergence. Figure 2 expresses the steps of the solution approach by computer. To check the validity of the present model, the numerical results for the first and second solutions are compared with Bhattacharyya [35] and Lok et al. [36] which is illustrated in Table 1 in the absence of cross nanofluid, thermophoresis, Brownian motion and suction/injection. Further, it is observed that the obtained results are in good agreement with the results of Bhattacharyya [35] and Lok et al. [36]. To further strengthen the present result, the different values of Pr on the rate of heat transfer are compared with Mahapatre and Gupta [37] which is shown in Table 2. This evidence that the adopted numerical simulation gives precise results.

RESULTS AND DISCUSSION

The primary purpose of this portion is to express the Cross nanofluid transport behaviour on the flow of nanofluid over an extending/contracting sheet with the influence of slip mechanisms. In this study, temporal stability is accounted to find the physically realizable solution. Graphical outcomes are manifested in Figures 3-22 for velocity (f'), temperature (θ), concentration (χ), skin friction factor (C_f^*), rate of heat transfer (Nu^*) and rate of mass transfer (Sh^*) with the impacts of various active parameters such as extending/contracting surface parameter (λ_T), Weissenberg number (We), suction/injection parameter (f_w), Eckert number (E_C), Brownian movement parameter (N_B) and thermophoresis parameter (N_T). The system of non-dimensionalized equations has been computed by employing the RKF method. Solid and dash lines are used to represent the first solution and the second solutions of Cross nanofluid, respectively. It is noteworthy to mention that there exist two solutions for various values of λ_T. First and second solutions exist for $\lambda_T > \lambda_C$, unique solution exists for $\lambda_T = \lambda_c$ and there is no solution for $\lambda_T > \lambda_c$ where lower script c denotes the critical value.

Figure 3 discloses the changes in dimensionless local skin friction coefficient (C_f^*) for increasing values of extending/contracting surface parameter (λ_T) and Weissenberg number (We). It is observed from this figure that there are two solutions exist for $\lambda_c < \lambda_T < 0$, and the critical values of λ_T are $\lambda_c \approx -1.306, -1.314, -1.330$. Further, it is noticed that increasing values of We tend to decline skin friction at the surface for both first and second solutions. Figure 4 depicts the effects of extending/contracting surface parameter (λ_T) and power law index (n_k) on dimensionless local skin friction coefficient (C_f^*).
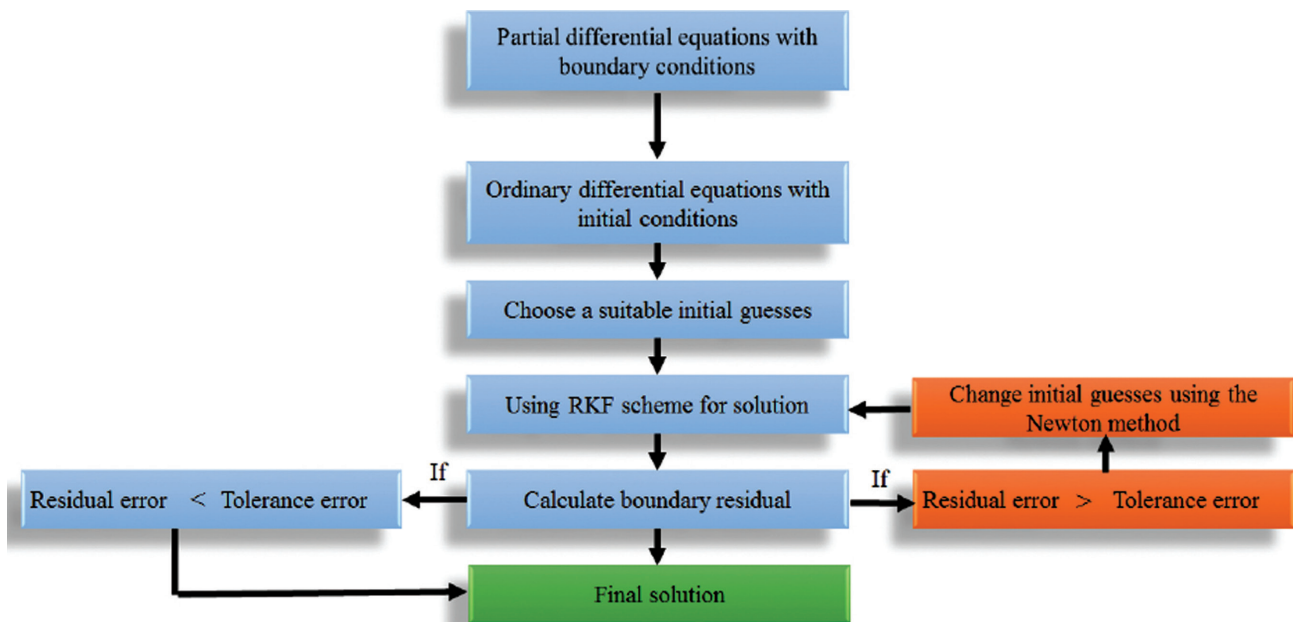

Figure 2. Solution approach by computer.

Table 1. Comparison results of λ_T on dual nature $f''(0)$ when $n_k = 1$ and $We = N_B = N_T = f_W = 0$

Parameter	Bhattacharyya [35]		Lok et al. [36]		Present	
λ_T	First solution	Second solution	First solution	Second solution	First solution	Second solution
1			0	-	0	-
0.5			0.713295		0.713294	-
0			1.232558		1.232556	-
−1.15	1.0822316	0.1167023			1.0822318	0.1167029
−1.2	0.9324728	0.2336491			0.9324729	0.2336493
−1.24657	0.5745268	0.5639987			0.5745262	0.5639980

Table 2. Comparison results of Pr on $\theta'(0)$ when $n_k = \lambda_T = 1$ and $we = N_B = N_T = f_W = 0$

Parameter	Values	Mahapatre and Gupta[37]	Present Result
Pr	0.05	−0.178	−0.178412
	0.5	−0.563	−0.564190
	1.0	−0.796	−0.797885
	1.5	−0.974	−0.977207

In this plot, we can notice that the critical values decline from $\lambda_c \approx -1.325$ to -1.340 for uplifting values of n_k. It is also observed that both the solutions augment the skin friction because larger n_k values provide a high friction in Cross nanofluid. Various values of extending/contracting surface parameter (λ_T) and suction or injection parameter (f_w) on dimensionless local skin friction coefficient (C_f^*) is displayed in Fig. 5. It is seen that the first solution enhances skin friction but the second solution declines skin friction. The related critical values corresponding to λ_T are $\lambda_c \approx -1.330, -1.450, -1.600$.

Figure 6 manifest the influence of Brownian movement parameter (N_B) and extending/contracting surface parameter (λ_T) on dimensionless local rate of heat transfer (Nu^*). This graph reveals that both solutions tend to decline the rate of heat transfer on the surface. The critical values of λ_T are the same as $\lambda_c \approx -1.330$ for higher values of N_B. Figure 7 exhibits the changes in dimensionless local rate of heat transfer (Nu^*) for several values of extending/contracting surface parameter (λ_T) and thermophoresis parameter (N_T). It is evident from this figure that two solutions exist for the same critical value $\lambda_c \approx -1.330$ of λ_T. From this figure, it is seen that Nu^* declines for uplifting N_T for the first and second solutions. Figure 8 displays the variation of Nu^* against λ_T for $E_c = 0, 0.2, 0.4$. It is clarified from Fig. 8 that λ_T has the same critical point $\lambda_c \approx -1.330$ as E_c uplifts from 0 to 0.4. Further, increasing the values of E_c decline the rate of heat transfer at the surfaces for first and second solutions. Changes in dimensionless local rate of mass transfer (Sh^*) due to Brownian movement parameter (N_B), extending/contracting surface parameter (λ_T) and thermophoresis parameter (N_T) are plotted in Figs. 9 and 10, respectively. It is important to note that both figures have the same critical point $\lambda_c \approx -1.328$ for the given values of N_B and N_T. In Fig. 9, both the solutions lessens the rate of mass transfer for uplifting N_B while an opposite behavior is observed in Fig. 10 for higher values of N_T.

Figures 11 and 12 are drawn to portray the impact of Weissenberg number (We) on velocity (f') and temperature (θ). It is evident from these figures that the first and second solutions have a similar nature. Moreover, increasing values of We leads to decrease the material relaxation time, which in turn increase the nanofluid velocity and decrease the temperature. Effect of Eckert number on θ for the first and second solutions is plotted in Fig. 13. It is noticed that enhancing E_c tends to elevate the internal source of energy which results in enhancing the thermal boundary layer. Figures 14–16 are sketched to explore the influence of suction parameter (f_w) on velocity (f'), temperature (θ) and concentration (χ) distributions, respectively. The effect of f_w on f' is divulged in Figure 14. The Cross nanofluid velocity is increased by raising the fluid injection in the cases of first solution. In general, the momentum diffusivity is rising when enhancing the fluid injection. Figure 15 demonstrates the impact of f_w on θ. The fluid temperature for a stable solution case is lessened for the higher values of f_w; however reverse trend for second solution. Effect of f_w on χ is plotted in Fig. 16. There is a decay in χ when f_w is rising, because injecting fluid at the surface which highly diminishes the mass related boundary layer thickness but the opposite nature is observed for the second solution.

The variation of extending/contracting surface parameter (λ_T) on velocity (f') and temperature (θ) are displayed in Figs. 17 and 18, respectively. Figure 17 portrays that f' shows an increasing nature for higher values of λ_T in the

stable solution. In contrast, the second solution of Cross nanofluid velocity expresses the decreasing behavior. Figure 18 displays the influence of λ_T on θ. It is evident for the stable solution that the thermal related boundary layer thickness is slightly decreasing with enhancing values of λ_T while an opposite trend is observed for the second solution. First and second solutions on dimensionless local rate of heat transfer (Nu^*) are sketched in Figs. 19-22 for various values of extending/contracting surface parameter (λ_T), Eckert number (E_c) and thermophoresis parameter (N_T). 25 × 25 meshes are considered to plot the 3D-surface and contour figures. Form Figs. 19 and 22, it is noticed that λ_T has the same critical point $\lambda_c \approx -1.330$. It is seen from these figures that both solutions decline the rate of heat transfer with an increase in E_c and N_T. Table 3 manifests the least eigenvalues for different values of We from the first and second solutions. It is observed that γ expresses the positive and negative values for the first solution and the second solution cases, respectively. It is revealed that the first solution over an extending/contracting sheet is stable while another solution is unstable.

Table 3. The smallest eigenvalues γ for $We = 0.8, 0.9$

Parameter	Values	λ_T	γ	
			First solution	**Second solution**
		−1.300	1.3780	−0.3964
		−1.290	1.4050	−0.4545
		−1.280	1.4260	−0.4859
		−1.270	1.4440	−0.5216
		−1.260	1.4590	−0.5425
	0.8	−1.250	1.4720	−0.5535
		−1.230	1.4950	−0.7486
		−1.220	1.5050	−0.8496
We		−1.210	1.5140	−1.0510
		−1.200	1.5230	−2.8580
		−1.300	1.3820	−0.3573
		−1.290	1.4010	−0.3675
		−1.280	1.4170	−0.3872
	0.9	−1.270	1.4300	−0.4280
		−1.260	1.4420	−0.4461
		−1.250	1.4520	−0.5443
		−1.220	1.4730	−0.7041

CONCLUSION

The current numerical study has been carried out to scrutinize the dual natures and stability analysis of Cross nanofluid with the influence of thermophoresis and Brownian motion. It is important to mention that two solutions are obtained for a limited range of extending/contracting parameter on the surface. Graphical representations are presented (two-dimensional plot, contour plot and three-dimensional surface plot) to characterize the velocity, temperature, concentration, skin friction factor, heat transfer
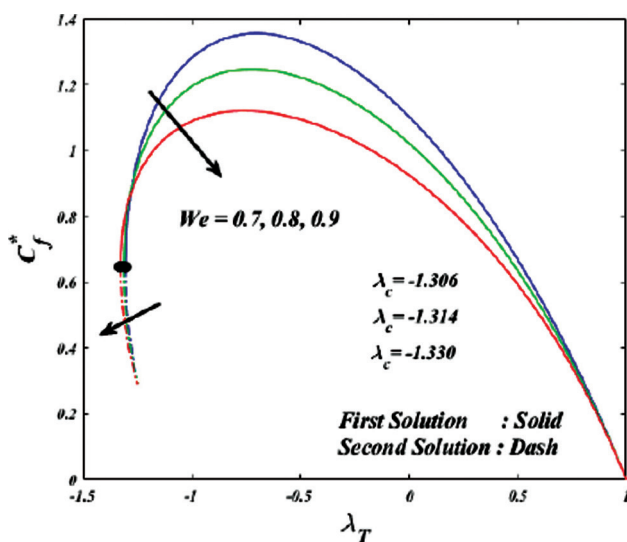

**Figure 3.** Effects of λ_T and We on C_f^*.
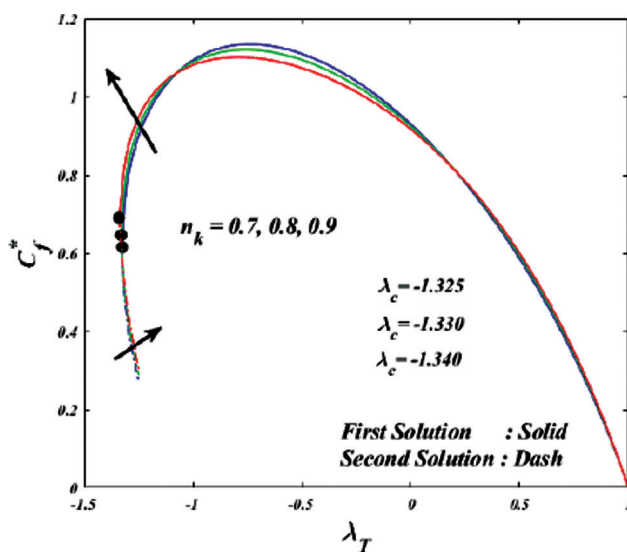
Figure 4. Effects of λ_T and n_k on C_f^*.

rate, and mass transfer rate. The important results are listed as follows:

- Injecting the Cross fluid on the surface is enhancing the nanofluid velocity for the first solution.
- Growing values of Weissenberg number uplift Cross fluid temperature in both cases.
- Increasing values of Eckert number tends to uplift the Cross nanofluid temperature.
- The Cross nanofluid temperature augments when contracting the surface for the first solution but reverse nature is found for the second solution.
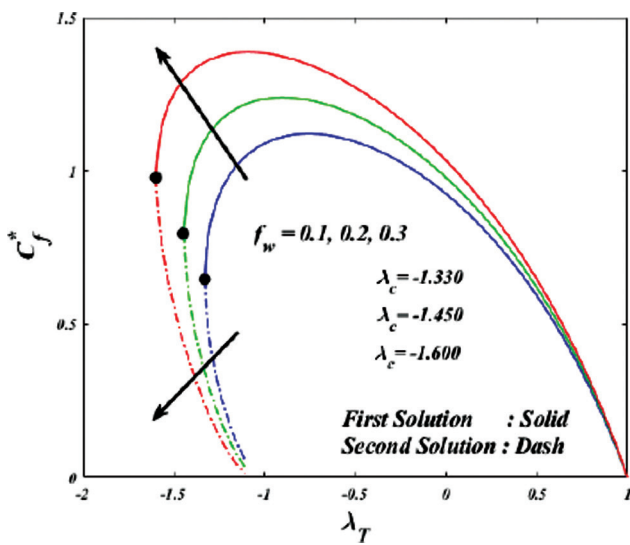
Figure 7. Effects of λ_T and N_T on Nu^*.
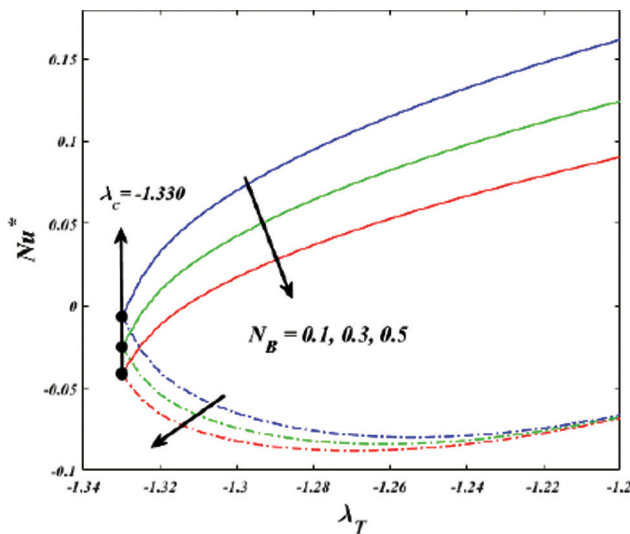
Figure 5. Effects of λ_T and f_w on C_f^*.
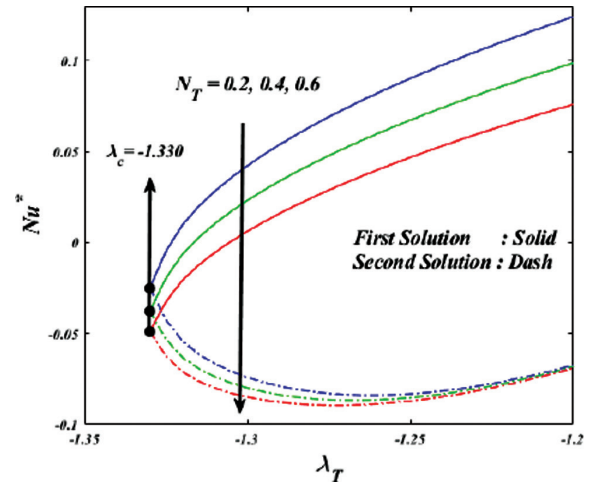
Figure 8. Effects of λ_T and E_c on Nu^*.
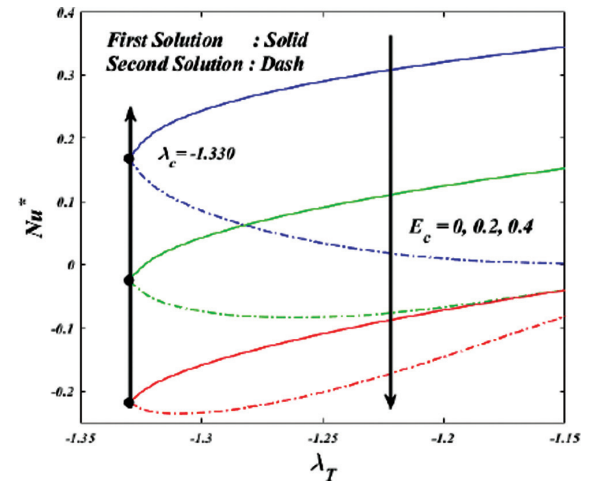
Figure 6. Effects of λ_T and N_B on Nu^*.
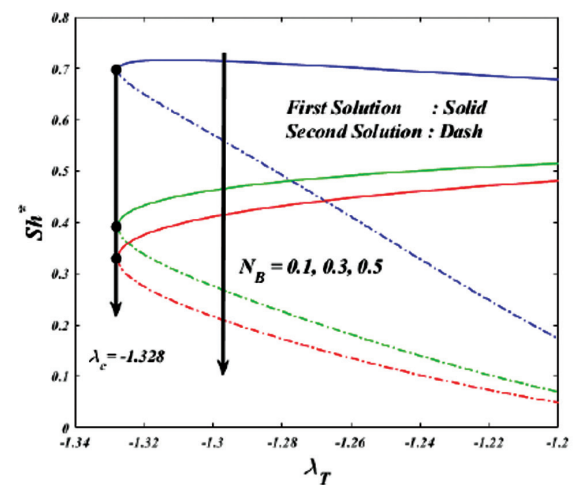
Figure 9. Effects of λ_T and N_B on Sh^*.

- Weissenberg number has an opposite nature on skin friction for the first and second solutions.
- Heat and mass transfer rates express the same critical point with the impact of Brownian motion and thermophoresis.
- In this model, it is clear that the first solution is physically realizable and stable.

NOMENCLATURE

x and y space coordinates
u and v velocity components along the x and $y-$ directions
C_w wall concentration
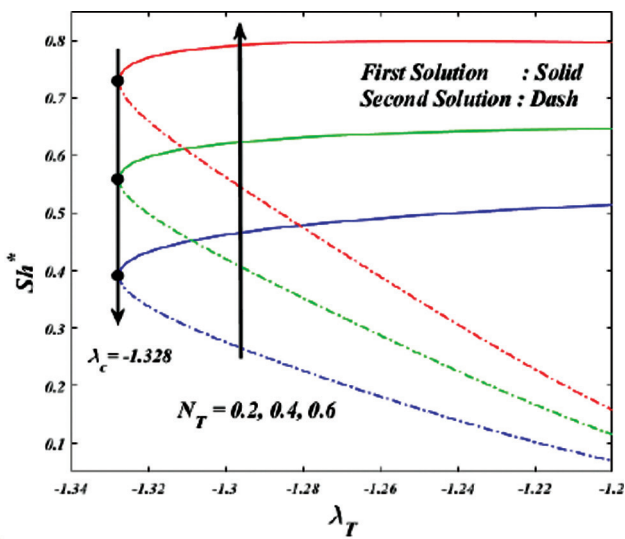
Figure 10. Effects of λ_T and N_T on Sh^*.
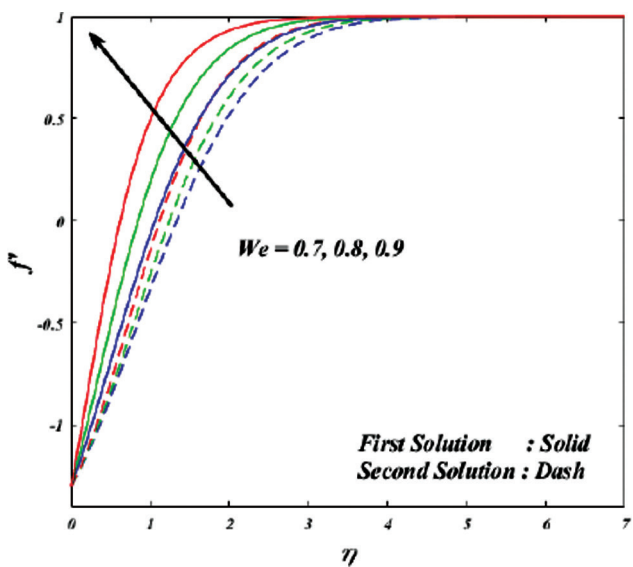
Figure 11. Effect of We on f'.
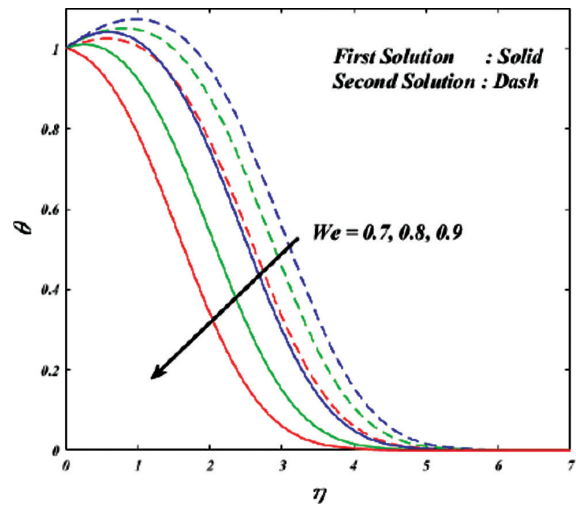
Figure 12. Effect of We on θ.
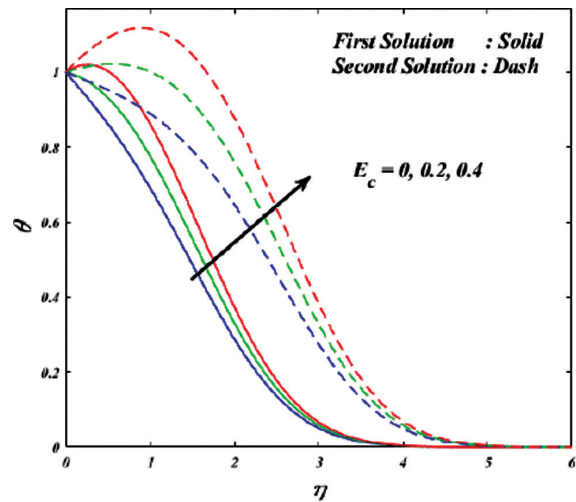
Figure 13. Effect of E_c on θ.
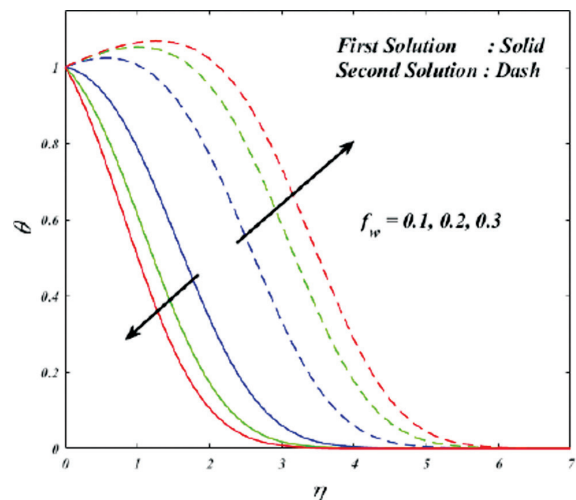
Figure 14. Effect of f_w on f'.
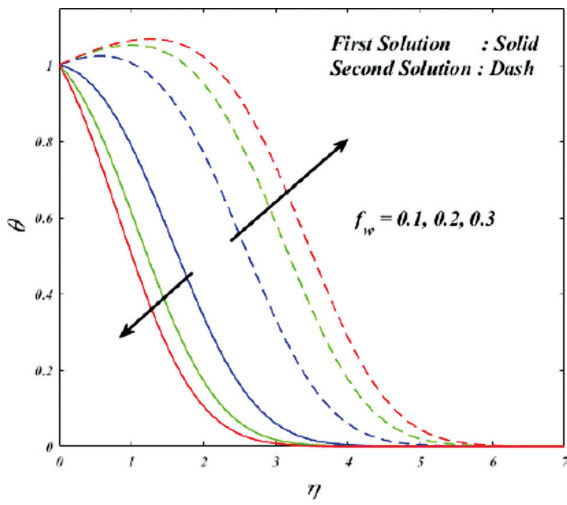
Figure 15. Effect of f_w on θ.
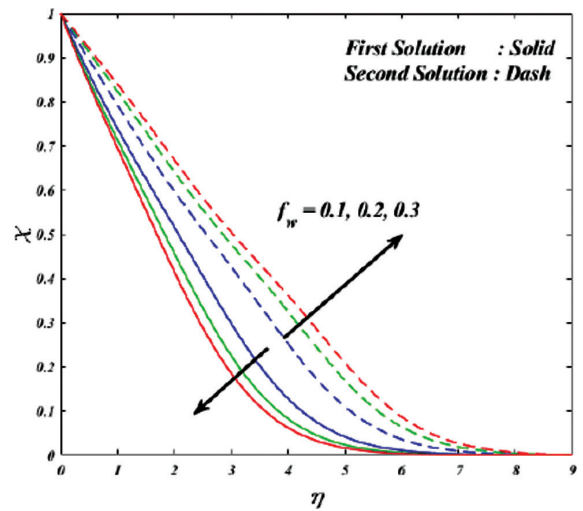
Figure 16. Effect of f_w on χ.
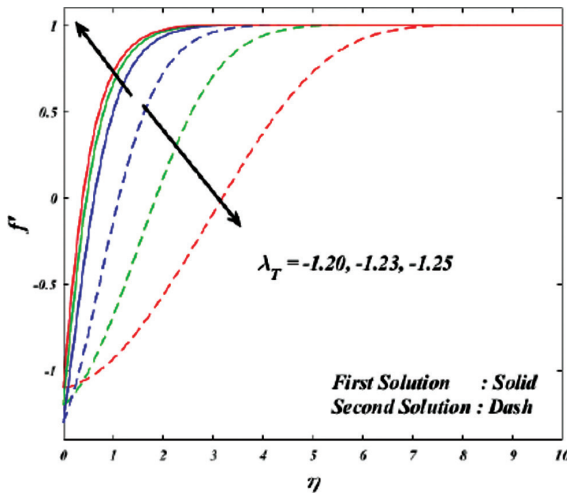
Figure 17. Effect of λ_T on f'.
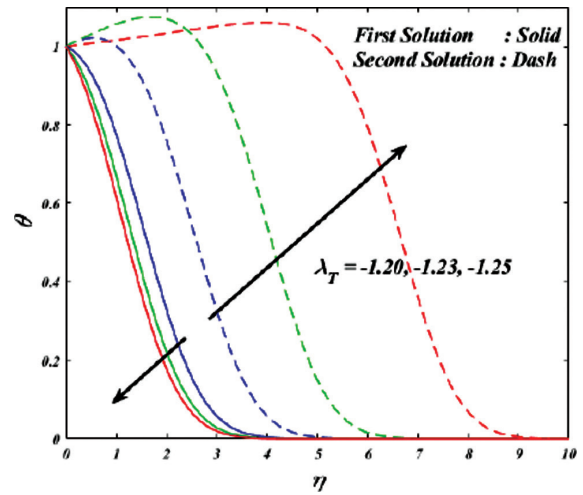
Figure 18. Effect of λ_T on θ.
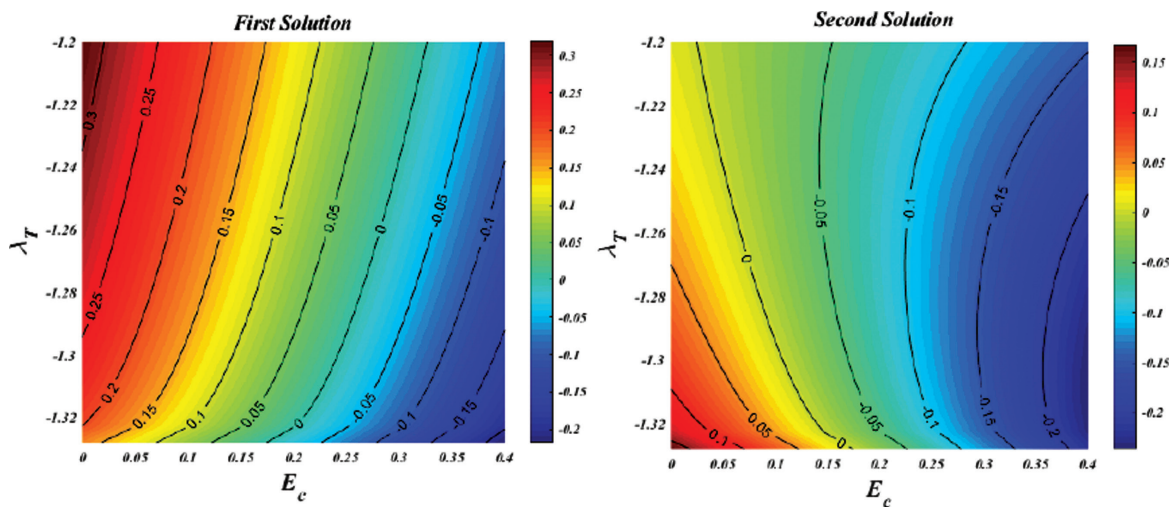
Figure 19. Effects of λ_T and E_C on Nu^*.
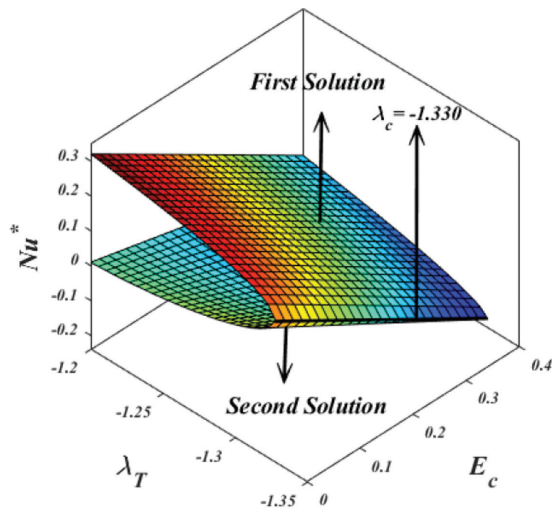
Figure 20. Effects of λ_T and E_C on Nu^*.
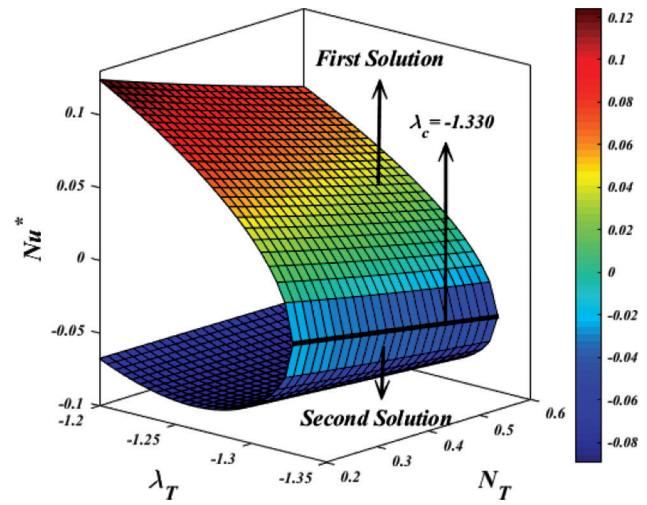
Figure 22. Effects of λ_T and N_T on Nu^*.
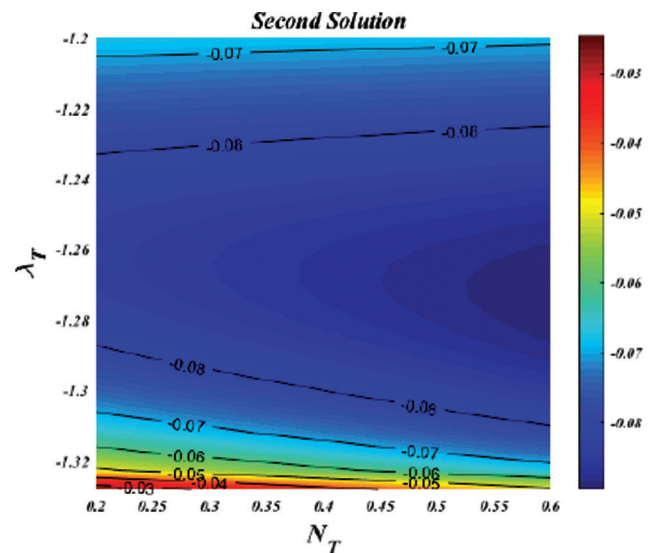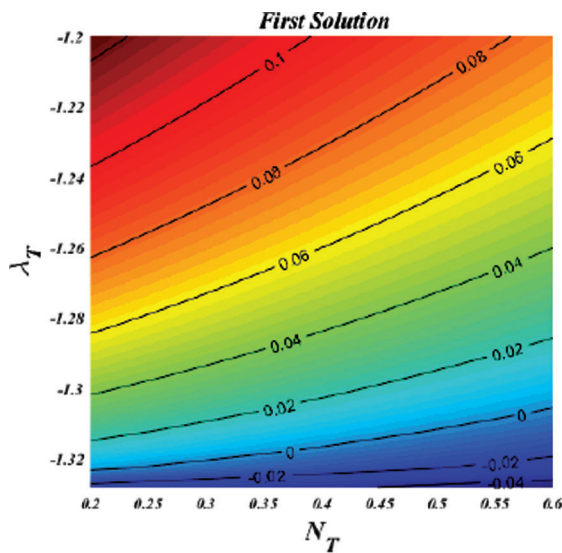
Figure 21. Effects of λ_T and N_T on Nu^*.

C	fluid concentration
C_∞	ambient concentration
T_∞	ambient temperature
T_w	wall temperature
T	fluid temperature
u_w	velocity of extending/contracting surface
u_e	free stream velocity
n_k	power law index
k_f	fluid thermal conductivity
$(C_p)f$	specific heat capacity of fluid
D_B	Brownian diffusion
D_T	thermophoretic diffusion
V_w	suction/injection parameter

We	Weissenberg number
Pr	Prandtl number
N_B	Brownian movement parameter
N_T	thermophoresis parameter
E_c	Eckert number
Sc	Schmidt number.
C_f^*	dimensionless local skin friction coefficient
Nu^*	dimensionless local rate of heat transfer
Sh^*	dimensionless local rate of mass transfer

Greek symbols

λ_T	extending/contracting surface parameter
v_f	kinematic viscosity

τ	ratio between nanoparticle and base fluid
$\tau^\star$	dimensionless time dependent variable
μ_f	dynamic viscosity
ρ_f	density of fluid
Γ	material parameter
$\alpha^\star$	thermal diffusivity

AUTHORSHIP CONTRIBUTIONS

Authors equally contributed to this work.

DATA AVAILABILITY STATEMENT

The authors confirm that the data that supports the findings of this study are available within the article. Raw data that support the finding of this study are available from the corresponding author, upon reasonable request.

CONFLICT OF INTEREST

The author declared no potential conflicts of interest with respect to the research, authorship, and/or publication of this article.

ETHICS

There are no ethical issues with the publication of this manuscript.

REFERENCES

[1]   Basha HT, Sivaraj R, Reddy AS, Chamkha AJ. SWCNH/diamond-ethylene glycol nanofluid flow over a wedge, plate and stagnation point with induced magnetic field and nonlinear radiation – solar energy application. Eur Phys J Spec Top 2019;228**:**2531–2551. [CrossRef]

[2]   Hatami M, Hatami J, Ganji DD. Computer simulation of MHD blood conveying gold nanoparticles as a third grade non-Newtonian nanofluid in a hollow porous vessel. Comput Methods Programs Biomed 2013;113:632–641. [CrossRef]

[3]   Said Z, Assad MEH, Hachicha AA, Bellos E, Ali M, Zeyad D, et al. Enhancing the performance of automotive radiators using nano fluids. Renew Sustain Energy Rev 2019;112:183–194. [CrossRef]

[4]   Buongiorno J. Convective Transport in Nanofluids. J Heat Transf 2006;128:240–250. [CrossRef]

[5]   Basha HT, Sivaraj R, Animasaun IL, Makinde OD. Influence of non-uniform heat source/sink on unsteady chemically reacting nanofluid flow over a cone and plate. Defect Diffus Forum 2018;389:50–59. [CrossRef]

[6]   Pal D, Roy N, Vajravelu K. Thermophoresis and Brownian motion effects on magneto-convective heat transfer of viscoelastic nanofluid over a stretching sheet with nonlinear thermal radiation. Int J Amb Energy 2019;1–12. [CrossRef]

[7]   Mittal AS, Patel HR. Influence of thermophoresis and Brownian motion on mixed convection two dimensional MHD Casson fluid flow with nonlinear radiation and heat generation, Physica A 2019;537:122710. [CrossRef]

[8]   Riaz A, Gul A, Khan I, Ramesh K, Khan SU, Baleanu D, et al. Mathematical analysis of entropy generation in the flow of viscoelastic nanofluid through an annular region of two asymmetric annuli having flexible surfaces. Coatings 2020;10:213. [CrossRef]

[9]   Makinde OD, Khan WA, Khan ZH. Stagnation point flow of MHD chemically reacting nanofluid over a stretching convective surface with slip and radiative heat. Proc Inst Mech Eng E 2017;231:695–703. [CrossRef]

[10] Rehman KU, Khan AA, Malik MY, Makinde OD. Thermophysical aspects of stagnation point magnetonanofluid flow yields by an inclined stretching cylindrical surface: a non-Newtonian fluid model. J Braz Soc Mech Sci Eng 2017;39:3669–3682. [CrossRef]

[11] Khan WA, Makinde OD, Khan ZH. Non-aligned MHD stagnation point flow of variable viscosity nanofluids past a stretching sheet with radiative heat. Int J Heat Mass Transf 2016;96:525–534. [CrossRef]

[12] Ibrahim W, Makinde OD. Magnetohydrodynamic stagnation point flow and heat transfer of Casson nanofluid past a stretching sheet with slip and convective boundary condition. J Aerosp Eng 2016;29:04015037. [CrossRef]

[13] Basha HT, Sivaraj R, Reddy AS, Chamkha AJ, Tilioua M. Impacts of temperature-dependent viscosity and variable Prandtl number on forced convective Falkner–Skan flow of Williamson nanofluid. SN Appl Sci 2020;2**:**477. [CrossRef]

[14] Khan AU, Hussain ST, Nadeem S. Existence and stability of heat and fluid flow in the presence of nanoparticles along a curved surface by mean of dual nature solution. Appl Math Comput 2019;353:66–81. [CrossRef]

[15] Pop I, Naganthran K, Nazar R. Numerical solutions of non-alignment stagnation-point flow and heat transfer over a stretching/shrinking surface in a nanofluid. Int J Numer Methods Heat Fluid Flow 2016;26:1747–1767. [CrossRef]

[16] Mahapatra TR, Sidui S. Unsteady heat transfer in non-axisymmetric Homann stagnation-point flows towards a stretching/shrinking sheet. Eur J Mech B Fluids 2019; 75:199–208. [CrossRef]

[17] Hashim, Khan M, Khan U. Stability analysis in the transient flow of Carreau fluid with non-linear

radiative heat transfer and nanomaterials: Critical points. J Mol Liq 2018; 272:787–800. [CrossRef]

[18] Hamid A, Khan M, Hafeez A. Unsteady stagnation-point flow of Williamson fluid generated by stretching / shrinking sheet with Ohmic heating. Int J Heat Mass Transf 2018;126:933–940. [CrossRef]

[19] Alam MS, Khatun MA, Rahman MM, Vajravelu K. Effects of variable fluid properties and thermophoresis on unsteady forced convective boundary layer flow along a permeable stretching/shrinking wedge with variable Prandtl and Schmidt numbers. Int J Mech Sci 2016;105:191–205. [CrossRef]

[20] Bachok N, Ishak A, Pop I. Melting heat transfer in boundary layer stagnation-point flow towards a stretching / shrinking sheet. Phys Lett A 2010; 374:4075–4079. [CrossRef]

[21] Dogonchi AS, Ganji DD. Investigation of MHD nano fluid flow and heat transfer in a stretching / shrinking convergent / divergent channel considering thermal radiation. J Mol Liq 2016;220:592–603. [CrossRef]

[22] Kumar BR, Sivaraj R. Heat and mass transfer in MHD viscoelastic fluid flow over a vertical cone and flat plate with variable viscosity. Int J Heat Mass Transf 2013;56:370–379. [CrossRef]

[23] Sivaraj R, Kumar BR. Unsteady MHD dusty viscoelastic fluid Couette flow in an irregular channel with varying mass diffusion. Int J Heat Mass Transf 2012;55:3076–3089. [CrossRef]

[24] Benazir AJ, Sivaraj R, Rashidi MM. Comparison between casson fluid flow in the presence of heat and mass transfer from a vertical cone and flat plate. J Heat Transfer 2016;138:112005. [CrossRef]

[25] Mythili D, Sivaraj R. Influence of higher order chemical reaction and non-uniform heat source / sink on Casson fluid flow over a vertical cone and flat plate. J Mol Liq 2016;216:466–475. [CrossRef]

[26] Cross MM. Rheology of non-Newtonian fluids: A new flow equation for pseudoplastic systems. J Colloid Sci 1965;20:417–437. [CrossRef]

[27] Abbas SZ, Khan WA, Sun H, Ali M, Irfan M, Shahzed M, et al. Mathematical modeling and analysis of Cross nanofluid flow subjected to entropy generation. Appl Nanosci 2019;10:3149–3160. [CrossRef]

[28] Khan IM, Hayat T, Imran M, Alsaedi A. Activation energy impact in nonlinear radiative stagnation point flow of Cross nano fluid. Int Commun Heat Mass Transf 2018; 91: 216–224. [CrossRef]

[29] Azam M, Xu T, Shakoor A, Khan M. Effects of Arrhenius activation energy in development of covalent bonding in axisymmetric flow of radiative-Cross nanofluid. Int Commun Heat Mass Transf 2020;113:104547. [CrossRef]

[30] Shahzad M, Sun H, Sultan F, Khan WA, Ali M, Irfan M. Transport of radiative heat transfer in dissipative Cross nanofluid flow with entropy generation and activation energy. Phys Scr 2019;94:115224. [CrossRef]

[31] Makinde OD. On the Chebyshev collocation spectral approach to stability of fluid flow in a porous medium. Int J Numer Meth Fluids 2009;59:791–799. [CrossRef]

[32] Makinde OD. Stagnation point flow with heat transfer and temporal stability of ferrofluid past a permeable stretching/shrinking sheet. Defect Diffus Forum 2018;387:510–522. [CrossRef]

[33] Hashim, Khan M, Alshomrani AS, Haq RU. Investigation of dual solutions in flow of a non-Newtonian fluid with homogeneous–heterogeneous reactions: Critical points. Eur J Mech B-Fluid 2018;68:30–38. [CrossRef]

[34] Harris SD, Ingham DB, Pop I. Mixed convection boundary-layer flow near the stagnation point on a vertical surface in a porous medium: Brinkman model with slip. Transp Porous Med 2009;77:267–285. [CrossRef]

[35] Bhattacharyya K. Dual solutions in unsteady stagnation-point flow over a shrinking sheet. Chin Phys Lett 2011;28:084702. [CrossRef]

[36] Lok YY, Ishak A, Pop I. MHD stagnation-point flow towards a shrinking sheet. Int J Numer Methods Heat Fluid Flow 2011;21:61–72. [CrossRef]

[37] Mahapatra T, Gupta A. Heat transfer in stagnation-point flow towards a stretching sheet. Heat Mass Transf 2002;38:517–521. [CrossRef]